Simultaneous materials and layout optimization of non-imaging optically concentrated solar thermoelectric generators

Gaetano Contento[a,*], Bruno Lorenzi[b], Antonella Rizzo[a], Dario Narducci[b]

[a] *ENEA – Italian National Agency for New Technologies, Energy and Sustainable Economic Development, Brindisi Research Centre, SS 7 Appia km 706, I–72100 Brindisi, Italy*
[b] *Dept. of Materials Science, University of Milano Bicocca, via R. Cozzi 55, I–20125 Milan, Italy*

Abstract

A 4×-non-imaging optically concentrated solar thermoelectric generator (STEG) was simulated and its layout was optimized depending on materials characteristics. The performances of seven state-of-the-art thermoelectric materials were realistically compared considering direct normal irradiances (DNI) between 400 and 900 W/m^2 and temperature dependence of the thermoelectric parameters. The model was tested with experimental data from literature and leg aspect ratios, fill factor (or thermal concentration), and leg number per STEG unit area were also used as variables. Due to the high values of thermal concentrations at maximum efficiency, different materials filling the gap among STEG legs were also considered. Maximum efficiency weakly decreases for filler thermal conductivities typical of common insulating materials for filler thermal conductivities typical of common insulating materials, opening novel opportunities for STEGs not requiring vacuum. Results of the analysis show that skutterudites, lead telluride and bismuth telluride exhibit the highest efficiencies ($\approx 7\%$) in the studied range of thermal concentrations and for a DNI equal to 900 W/m^2. However, skutterudites and lead telluride were found to be very sensitive on the DNI level, differently from bismuth telluride, which therefore qualifies as the best solution for energy conversion. Moreover, optimal layouts for STEGs based on bismuth telluride more easily meet manufacturing constraints.

Keywords: Solar thermoelectric generation, Thermoelectricity, Thermoelectric materials, Thermal concentration, Solar concentration, Solar energy.

List of Symbols

---

[*] Corresponding author

A_{sh}	Area interested by shunt heat losses due to conduction through filler or irradiation, m^2
A	Selective absorber area, m^2
A_{enc}	External area of the vacuum tube, m^2
$A_{\mathrm{n,p}}$	n,p-type leg cross sectional area, m^2
C_{geo}	Geometrical concentration
F	TEG device fill factor
$G(DNI)$	Direct solar irradiance, $\frac{\mathrm{W}}{\mathrm{m}^2}$
$I_{\mathrm{n,p}}$	n,p-type leg current, A
J	Leg current density, $\frac{\mathrm{A}}{\mathrm{m}^2}$
$K_{\mathrm{rad,SSA}}$	Radiative thermal conductance between SSA and vacuum tube, $\frac{\mathrm{W}}{\mathrm{K}}$
$K_{\mathrm{rad,TEG}}$	Radiative thermal conductance between the facing hot-side and cold-side of the TEG, $\frac{\mathrm{W}}{\mathrm{K}}$
$K_{\mathrm{rad,enc}}$	Radiative thermal conductance of the evacuated tube external surface, $\frac{\mathrm{W}}{\mathrm{K}}$
$K_{\mathrm{sc+Cu}}$	Metallic contact and substrate spreading-constriction thermal conductance at the hot side and cold side of the TEG, $\frac{\mathrm{W}}{\mathrm{K}}$
K_{teg}	Thermal conductance of the thermocouple, $\frac{\mathrm{W}}{\mathrm{K}}$
$L_{\mathrm{n,p}}$	n,p-type leg length, m
N_{tc}	Number of thermocouples
$P^{\mathrm{in}}_{\mathrm{TEG}}$	Power absorbed by selective absorber of the TEG hot-side, W
P_{out}	Electrcal output power, W
Q_{h}	Heat flowing within the TEG from its hot plate, W
R	TEG internal resistance, Ω
R_{L}	Load resistance, Ω
S	CPC aperture area, m^2
$S_{\mathrm{n,p}}$	n,p-type material Seebeck coefficient, $\frac{\mathrm{V}}{\mathrm{K}}$
$T_{\mathrm{c,h}}$	TEG cold-side (hot-side) temperature, K
T_{enc}	Temperature of the encapsulation, K
T_{s}	Temperature of the SSA, K
U_{hs}	heat sink thermal coefficient, $\frac{\mathrm{W}}{\mathrm{K}}$
V_{oc}	Open circuit voltage, V
$W_{\mathrm{J,n-p}}$	n,p-type Joule weight factors,
$W_{\mathrm{T,n-p}}$	n,p-type Thomson weight factors,
d_{x}	Thickness of a substrate x, m
h	Convective heat loss coefficient, $\frac{\mathrm{W}}{\mathrm{m}^2\mathrm{K}}$
$k_{\mathrm{n,p}}$	n,p-type material thermal conductivity, $\frac{\mathrm{W}}{\mathrm{mK}}$
k_{x}	Thermal conductivity of a substrate x, $\frac{W}{mK}$
m	R_{L}/R ratio
m_{opt}	Optimum value of m for maximum efficiency
n_{tc}	Thermocouples density on TEG, $\frac{1}{\mathrm{m}^2}$
r	Characteristic geometrical ratio between length and cross-sectional areas of TC legs, $\frac{1}{\mathrm{m}}$
v	Wind velocity, $\frac{\mathrm{m}}{\mathrm{s}}$

Greek Symbols

α_{SSA}	Solar Selective Absorber (SSA) coefficient
β_{e}	Characteristic ratio of the legs lengths and cross-sections

ϵ_{enc}	External exposed encapsulation emissivity of the vacuum tube and the ambient
$\epsilon_{\mathrm{eq,SSA}}$	Equivalent emissivity between SSA and the facing surface of the enclosure
$\epsilon_{\mathrm{eq,sub}}$	Equivalent emissivity between the facing hot and cold-side plates of the TEG device
η_{c}	Carnot efficiency between T_{h} and T_{c}
η_{opt}	Optimum TEG efficiency
η_{ot}	Opto-thermal efficiency
$\eta_{\mathrm{TEG,tot}}$	Total efficiency of the thermoelectric device
η_{TEG}	Efficiency of the TEG
λ	Geometrical characteristic ratio to calculate the spreading/constriction resistance
ϕ	Spreading/constriction angle
$\rho_{\mathrm{n,p}}$	n,p-type material electrical resistivity, $\frac{\Omega}{\mathrm{m}}$
τ_{CPC}	Optical concentrator transmittance
τ_{enc}	Enclosure transmittance
$\tau_{\mathrm{n-p}}$	n,p-type Thomson coefficients, $\frac{\mathrm{V}}{\mathrm{K}}$
W_{el}	Useful electric power, W

Other Symbols

$[Z]^{*}_{\mathrm{eng}}$	TEG engineering figure of merit, K^{-1}

1. Introduction

Thermoelectric generators (TEGs) are being considered as an effective way to recover heat released from a host of sources. This has motivated a significant effort to develop novel, more efficient thermoelectric materials, leading to a highly diversified research on novel systems, both competing with bismuth telluride in the low-temperature range and extending the range of temperature over which thermoelectric generation may be carried out. Along this avenue, the thermoelectric figure of merit of *n*-PbTe, *n*-PbSe and *p*-PbTe were significantly improved over the last five years[1, 2], whereas enhanced performances were achieved with skutterudites [3, 4]. Also in the high-temperature range, nanostructured silicon-germanium bulk alloys are nowadays available for thermoelectric applications up to 900 °C [5, 6]. Impressive values of efficiency were also reported for *n*-$\mathrm{PbTe}_{1-x}\mathrm{I}_{x}$ and *p*-PbTe-SrTe in the intermediate temperature range [7, 8] along with the development of novel half-Heusler materials of *n* and *p* type [9, 10], to be used up to 700 °C.

The extended range of materials, the possibility to convert heat at moderately high temperatures, and the remarkable increase of thermoelectric efficiencies achieved over the last decade propelled novel applications.

Solar energy is a ubiquitous heat source that has attracted the attention of the thermoelectric community since Telkes' pioneering work [11]. In more recent times, TEGs have been reconsidered either as standalone solar harvesters [12, 13] or in hybrid devices including thermoelectric-PV [14–16] solar generators, co-generation systems [17], thermoelectric-thermophotovoltaic devices [18], and tri-generation cells [19]. Several solutions have been proposed to enhance the conversion efficiency while keeping materials use and costs low. They encompass optical concentration, thermal concentration, leg segmentation, vacuum enclosures (to reduce thermal losses), solar selective absorbers, and a more accurate selection of thermoelectric materials through realistic simulation of TEGs [20, 21].

Regarding the modelling of solar thermoelectric generators (STEGs), in the last ten years, several theoretical studies have been published in literature, often involving thin films [22–24]. Most of these works aimed to maximizing the efficiency of STEGs [25, 26], by focusing singly on the optimization of the thermoelectric material used [27, 28], or the design of the cooling system [29–31]. However, since the optimal thermal and optical design strictly depend upon materials characteristics, such kind of material-independent optimizations are bound not to attain the largest possible conversion efficiency.

To overcome this limitation in this paper we propose a novel approach to the design of solar thermoelectric harvesters based on the simultaneous optimization of materials and device layout. To this aim in this work we propose a model of a solar thermoelectric conversion system validated with the aid of some experimental results from the literature. Then we set to search for the optimal STEG by comparing singly optimized harvester layouts for seven high-efficiency materials, comparing their power outputs.

To this aim, it is mandatory to fully account for the temperature dependence of all transport coefficients [32], thus relaxing the constant-property approximation and using instead the formalism of the so-called engineering figure of merit [33, 34]. This revised figure of merit takes into account the important corrections due to Joule and Thomson effects, which can strongly affect the device power output as recently reported in several studies on TEGs performances [35, 36].

Layout optimization requires an analysis of thermal insulation among legs. However, it will be shown that vacuum is not mandatory to this aim, and that commercial insulating materials filling the gaps among STEG legs lead to efficiencies comparable to those attained under vacuum, with aerogels even outperforming it. This clearly impacts STEG manufacturability and costs.

Also, realistic modelling must account for DNI variability. Therefore, computations also investigated the effect of reduced irradiance on STEG efficiency. We anticipate that, although state-of-the-art skutterudites and lead telluride are the most efficient materials under standard irradiance conditions, their efficiencies severely drop for lower irradiances. Instead, bismuth telluride provides the best average performances, as its conversion efficiency remains almost constant, even when the irradiance becomes as low as 400 W/m^2.

2. STEG description

STEGs are made of five main parts (Figure 1): (1) an optical concentrator; (2) a solar selective absorber (SSA), converting the solar energy into heat and placed on the top of the TEG; (3) the TEG; (4) a suitable heat sink, dissipating heat at the TEG cold side; and (5) an enclosure (typically glass). The TEG was always encapsulated in an evacuated glass tube. While the whole TE module was always assumed to be encapsulated under vacuum, this assumptions was relaxed for the intraleg region. Two options were considered, namely that they were either under vacuum or filed with proper insulating materials.

2.1. *Optical and thermal concentration*

Optical concentration is largely used for solar applications, in particular in photovoltaic (PV) cells, to replace active (and expensive) materials with passive (and cheaper) reflective or refractive plastics or glass [37]. In solar thermal applications (as in thermoelectric conversion), the concentration increases the absorber temperature and the temperature difference along the thermocouples (TCs), therefore increasing conversion efficiencies [38]. Both imaging [39] and non-imaging [40, 41] optical concentrators can be used to this aim. With the latter option one can achieve lower concentrations and lower hot side temperatures [42, 43]. However, no high-precision sun-tracking systems are required [37], keeping low the overall cost and complexity of the system. So, the optical concentrator chosen for computations was a typical compound parabolic concentrator (CPC) [37, 42, 43]. More precisely, we considered a reflective 2-D CPC, namely a non-imaging concentrator mainly composed by two parabolic mirror segments that trap sun rays coming from any angle between the symmetry plane of CPC and the acceptance angle. The two faced segments of parabola reflect incoming light on the flat receiver located at the base of a trough-like geometry. Let S be the area of the entrance aperture of a CPC which concentrate the intercepted solar radiation onto a selective absorber of area A at the exit of the concentrator then,

$$C_{\mathrm{geo}} = \frac{S}{A} \tag{1}$$

is the geometrical concentration. More details about the CPC operating principles are reported elsewhere [37, 40]. In a similar way, one may also use thermal concentration [12, 38] to constrain the heat flow into the active materials, enabling reduced cross-section areas. This decreases the quantity of active material while increasing the temperature difference along the TC. Thus, higher conversion efficiency are obtained by reducing the materials costs — with an ultimate reduction of power costs.

2.2. *TEG layout*

The TEG devices are made of N_{tc} TCs soldered in between two facing substrates of alumina with area A, with the TCs connected in series by thin copper sheets. Thus, the number of TCs for unit TEG area is $n_{\mathrm{tc}} = N_{\mathrm{tc}}/A$. The n and p-type legs have cross-sectional areas A_{n} and A_{p} and lengths $L_{\mathrm{n}} = L_{\mathrm{p}} = L$, respectively.

We define the fill factor as.

$$F = \frac{N_{\mathrm{tc}}(A_p + A_n)}{A} \tag{2}$$

It is also useful to introduce a characteristic geometrical ratio,

$$r = \frac{L n_{\mathrm{tc}}}{F} \tag{3}$$

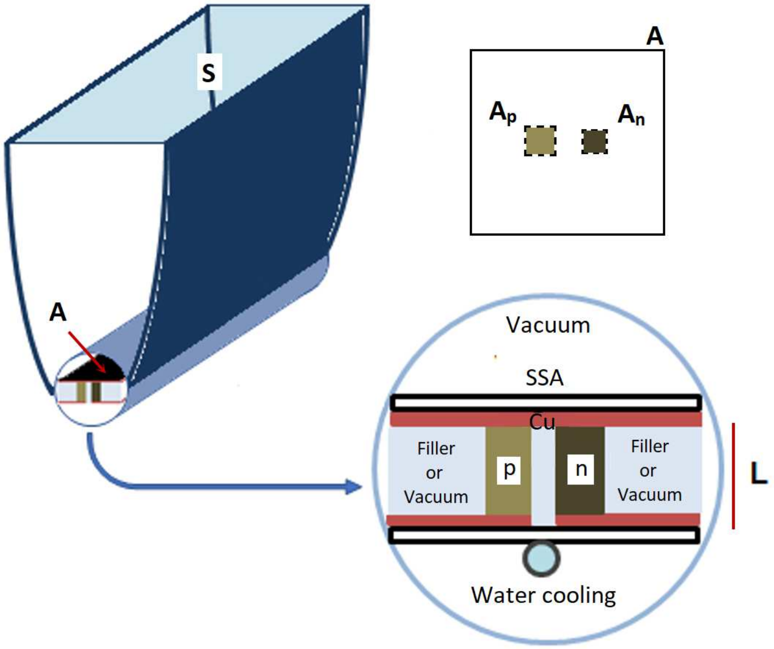

Figure 1: Scheme of the TEG system studied in this work. Note that generaly A_n and A_p have different values.

which conveniently groups the principal geometrical characteristics of a TEG. In turn, such ratio is equal to the geometrical aspect ratio of the legs, because $r = \frac{LC_\mathrm{geo}}{F(S/N_\mathrm{tc})} = \frac{L}{A_\mathrm{n} + A_\mathrm{p}}$. Thus, for any given materials, setting r also sets the electro-thermal properties of the TC legs.

In what follows we will consider the exemplar layout of a STEG (solar thermoelectric generator) wherein all TCs are aligned along a CPC trough (Figure 1) and have an intercepting area equal to $1/n_\mathrm{tc}$.

2.3. *Encapsulation*

In order to protect the TEG device from atmospheric agents and to thermally isolate it from the ambient, a good choice is to cover it with a glass enclosure under vacuum. In previous papers for PV-TE hybrid systems we considered a glass enclosure sitting at the entering aperture of the CPC [44, 45], also mechanically supporting the PV module. Here instead, we assume that a glass tube embeds only the TEG device with or without filler (Figure 1).

2.4. *Heat sinks*

In the thermal circuit the TEG cold plate is assumed to be in contact with a water-cooled heat sink. In a previous paper [45] we analysed the effect of both air-based and

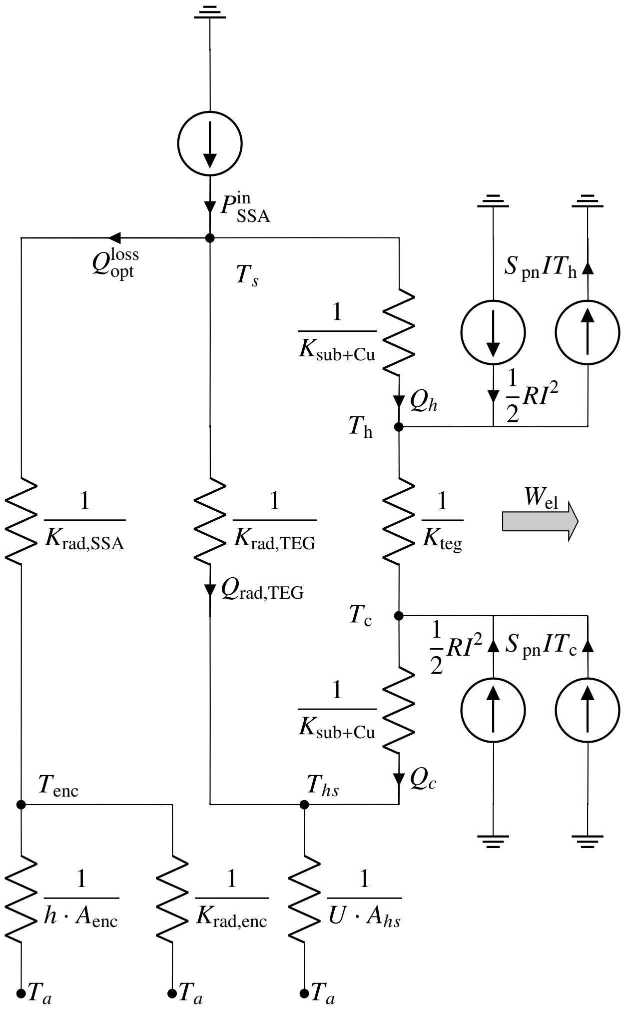

Figure 2: Thermal circuit of the system considered in this work. For simplicity here the case of constant Joule weight and no Thomson effect was considered.

water-based cooling on the energy production of a hybrid PV-TE system under concentrated sunlight, following the approach used by Yazawa *et al.* [46, 47]. It was shown that power consumption of water-based heat exchangers was negligible and that the efficiency of energy conversion reached a *plateau* for a value of the heat sink thermal coefficient U_{hs} of about 200 W/m^{2}K, easily reachable with water-cooling systems. As a result, in this study we kept fixed to 200 W/m^{2}K the heat sink thermal coefficient and we will neglect their power consumption in the forthcoming computations.

3. The model

3.1. Energy balance

If G is the solar irradiance and SG is the overall incoming solar power, the portion of the solar spectrum transmitted and concentrated by the glass tube and the CPC toward the SSA is,

$$P^{\mathrm{in}}_{\mathrm{SSA}} = \alpha_{\mathrm{SSA}}\tau_{\mathrm{cpc}}\tau_{\mathrm{enc}}SG \tag{4}$$

where α_{ssa} is the SSA absorption coefficient, τ_{CPC} is the CPC optical transmittance [48] and τ_{enc} is the enclosure transmittance.

However, only a fraction Q_{h} of the overall absorbed power flows through the TCs and is available for thermoelectric conversion due to radiative and convective losses from the SSA to the ambient, up through the CPC and the glass tube, and because of the shunts between facing hot and cold plates of the TEG. Thus, we define an opto-thermal efficiency η_{ot} as [12].

$$\eta_{\mathrm{ot}} = \frac{Q_{\mathrm{h}}(T_{\mathrm{h}}, T_{\mathrm{c}})}{SG} \tag{5}$$

As a consequence, if W_{el} is the useful electric power, the TEG total efficiency reads

$$\begin{aligned}\eta_{\mathrm{TEG,tot}}(T_{\mathrm{h}}, T_{\mathrm{c}}) = \frac{W_{\mathrm{el}}}{Q_{\mathrm{h}}(T_{\mathrm{h}}, T_{\mathrm{c}})}\frac{Q_{\mathrm{h}}(T_{\mathrm{h}}, T_{\mathrm{c}})}{SG} = \\ = \eta_{\mathrm{TEG}}(T_{\mathrm{h}}, T_{\mathrm{c}})\eta_{\mathrm{ot}}(T_{\mathrm{h}}, T_{\mathrm{c}})\end{aligned} \tag{6}$$

where η_{TEG} is the efficiency of the thermoelectric device [38, 45]. Manifestly enough, since $\eta_{\mathrm{TEG,tot}}$ is a function of the temperatures T_{h} and T_{c} at the TEG plates, its computation requires the solution of the pertinent thermal circuit problem (Figure 2).

The power balance at the SSA absorber with temperature T_{s} is

$$\begin{aligned}P^{\mathrm{in}}_{\mathrm{SSA}} - K_{\mathrm{rad,SSA}}(T_{\mathrm{s}}, T_{\mathrm{enc}})(T_{\mathrm{s}} - T_{\mathrm{enc}}) = Q_{\mathrm{h}}(T_{\mathrm{h}}, T_{\mathrm{c}}) + \\ + K_{\mathrm{rad,TEG}}(T_{\mathrm{h}}, T_{\mathrm{c}})(T_{\mathrm{h}} - T_{\mathrm{c}})\end{aligned} \tag{7}$$

where T_{enc} is the temperature of the evacuated tube (neglecting the thermal resistance of the glass). The second therm on the left-hand side of Equation (7) is the power lost by the SSA toward the glass tube, while on the right-hand side we have respectively the power entering the TEG device from the hot side, and that lost due to TEG shunts. In Equation (7) $K_{\mathrm{rad,SSA}}(T_{\mathrm{s}}, T_{\mathrm{enc}})$ and $K_{\mathrm{rad,TEG}}(T_{\mathrm{h}}, T_{\mathrm{c}})$ are respectively the radiative conductances of the thermal contacts between the SSA and the evacuated tube (i.e. facing hot and cold plates of the TEG devices) while $A_{\mathrm{sh}}(F, C_{\mathrm{geo}})$ is the effective area from which shunt losses take place [46]. All the functions here introduced are discussed and defined in Appendix A. It should be noted that in the second term on the right-hand side of Equation (7) we neglected both the substrate thermal resistance $1/K_{\mathrm{sub}}$ and the thermal cross-talk among legs (cf. Equation (A.7) and Figure 2).

Configurations where the gap among n and p legs is filled with a suitable insulating material were also considered. Fillers with temperature-independent thermal conductivity $k_{\rm filler}$ were considered. Thus, Equation (7) is replaced by.

$$P^{\rm in}_{\rm SSA} - K_{\rm rad,SSA}(T_{\rm s}, T_{\rm enc})(T_{\rm s} - T_{\rm enc}) = Q_{\rm h}(T_{\rm h}, T_{\rm c}) + \\ + \frac{k_{\rm filler} A_{\rm sh}(F, C_{\rm geo})}{L}(T_{\rm h} - T_{\rm c}) \quad (8)$$

At the $T_{\rm enc}$ node we have instead,

$$K_{\rm rad,SSA}(T_{\rm s}, T_{\rm enc})(T_{\rm s} - T_{\rm enc}) = hA_{\rm enc}(T_{\rm enc} - T_{\rm a}) + \\ + K_{\rm rad,enc}(T_{\rm enc}, T_{\rm a})(T_{\rm enc} - T_{\rm a}) \quad (9)$$

where $K_{\rm rad,enc}(T_{\rm enc}, T_{\rm a})$ and h are the radiative conductance of the external surface of the glass tube and its convective heat transfer coefficient, respectively; $T_{\rm a}$ is the ambient temperature; whereas $A_{\rm enc} = (\pi/2)A$ is the external area of the glass tube under vacuum (Figure 1). Whereas for TEG interfaces we write rispectively,

$$K_{\rm sc+Cu}(T_{\rm s} - T_{\rm h}) = Q_{\rm h}(T_{\rm h}, T_{\rm c}) \quad (10)$$

$$K_{\rm sc+Cu}(T_{\rm c} - T_{\rm hs}) = Q_{\rm c}(T_{\rm h}, T_{\rm c}) \quad (11)$$

where $K_{\rm sc+Cu}$ is the spreading-constriction conductance. It includes the conductances of the substrate and of the metallic contact [12] and, implicitly, takes into account the in-plane heat fluxes occurring through substrates and metal contacts (see Appendix B and [46] for further details). In view of the symmetry of the device, $K_{\rm sc+Cu}$ takes the same value at both sides of the TEG. Contact resistances between substrates and metal contact, and from this and TC legs were neglected. Finally, we consider the energy balance at the $T_{\rm hs}$ node. The power incoming from the shunt and that leaving the TEG cold side must equal the power removed by the heat sink,

$$U_{\rm hs}(T_{\rm hs} - T_{\rm a}) = Q_{\rm c}(T_{\rm h}, T_{\rm c}) + \\ + K_{\rm rad,TEG}(T_{\rm h}, T_{\rm c})(T_{\rm h} - T_{\rm c}) \quad (12)$$

where $U_{\rm hs}$ is the heat sink thermal coefficient.

Table 2 lists the TC materials used in the computations.

3.2. *TEG efficiency*

Since TEGs operate over large temperature differences, their modelling must take into account the temperature dependence of the materials thermoelectric properties. Following Kim *et al.* [33], the current density J is obtained by integrating twice the Domenicali equation for the n and the p-type leg,

$$\frac{d}{dx}\left(k(T)\frac{dT}{dx}\right) + J^2\rho(T) - J\tau(T)\frac{dT}{dx} = 0 \quad (13)$$

with boundary conditions $T(0) = T_\mathrm{h}$ and $T(L) = T_\mathrm{c}$.

The following expressions for the hot and cold side heat flux are obtained, with $I_\mathrm{p} = -I_\mathrm{n} = I$:

$$\begin{aligned} Q_\mathrm{h}(T_\mathrm{h}, T_\mathrm{c}) = N_\mathrm{tc} I T_\mathrm{h} \left(S_\mathrm{p}(T_\mathrm{h}) - S_\mathrm{n}(T_\mathrm{h})\right) + \\ N_\mathrm{tc} K_\mathrm{teg} \Delta T - N_\mathrm{tc}\left(W_\mathrm{J,p} R_\mathrm{p} + W_\mathrm{J,n} R_\mathrm{n}\right) I^2 - \\ N_\mathrm{tc} I \left(W_\mathrm{T,p} \int_{T_c}^{T_h} \tau_\mathrm{p}(T) dT - W_\mathrm{T,n} \int_{T_c}^{T_h} \tau_\mathrm{n}(T) dT\right) \end{aligned} \tag{14}$$

$$\begin{aligned} Q_\mathrm{c}(T_\mathrm{h}, T_\mathrm{c}) = N_\mathrm{tc} I T_\mathrm{c} \left(S_\mathrm{p}(T_\mathrm{c}) - S_\mathrm{n}(T_\mathrm{c})\right) + \\ N_\mathrm{tc} K_\mathrm{teg} \Delta T + N_\mathrm{tc} I \left((1 - W_\mathrm{J,p}) R_\mathrm{p} + (1 - W_\mathrm{J,n}) R_\mathrm{n}\right) I^2 + \\ N_\mathrm{tc} I \left((1 - W_\mathrm{T,p}) \int_{T_c}^{T_h} \tau_\mathrm{p}(T) dT - (1 - W_\mathrm{T,n}) \int_{T_c}^{T_h} \tau_\mathrm{n}(T) dT\right) \end{aligned} \tag{15}$$

where $\rho_\mathrm{n,p}$, $k_\mathrm{n,p}$ and $S_\mathrm{n,p}$ are the n, p-type electrical resistivities, thermal conductivities, and n, p-type Seebeck coefficients, respectively, while $\tau_\mathrm{n,p}$ are the n and p-type Thomson coefficients and $\Delta T = T_\mathrm{h} - T_\mathrm{c}$. Also,

$$I(T_\mathrm{h}, T_\mathrm{c}) = \frac{\left(\int_{T_c}^{T_h} S_\mathrm{p}(T) dT - \int_{T_c}^{T_h} S_\mathrm{n}(T) dT\right) \Delta T}{R(1 + m)} \tag{16}$$

is the current flowing into TCs connected in series whereas $m = R_\mathrm{L}/R$ is the ratio between the external load electrical resistance R_L and internal electrical resistance R.

The detailed expressions of the Joule and Thomson weight factors, $W_\mathrm{J,n-p}$ and $W_\mathrm{T,n-p}$, are reported in Appendix C. Suffice here to note that such definitions, along with Equation (14) and Equation (15), hold if the condition $\frac{dx}{dT} \simeq -\frac{L_\mathrm{p,n}}{\Delta T}$ is fulfilled.

The thermal conductance of a TC K_teg and the electrical resistance R are calculated taking into account the leg geometrical dimensions and the materials temperature-dependent properties.

$$K_\mathrm{teg} = \frac{1}{\Delta T}\left(\frac{A_\mathrm{p}}{L_\mathrm{p}} \int_{T_c}^{T_h} k_\mathrm{p}(T) dT + \frac{A_\mathrm{n}}{L_\mathrm{n}} \int_{T_c}^{T_h} k_\mathrm{n}(T) dT\right) \tag{17}$$

$$R = \frac{1}{\Delta T}\left(\frac{L_\mathrm{p}}{A_\mathrm{p}} \int_{T_c}^{T_h} \rho_\mathrm{p}(T) dT + \frac{L_\mathrm{n}}{A_\mathrm{n}} \int_{T_c}^{T_h} \rho_\mathrm{n}(T) dT\right) \tag{18}$$

The thermoelectric efficiency may be finally written using the engineering thermoelectric figure of merit $[Z]^*_\mathrm{eng}$.

$[Z]^{*}_{\mathrm{eng}} =$

$$= \frac{\left(\int_{T_c}^{T_h} S_{\mathrm{p}}(T)dT - \int_{T_c}^{T_h} S_{\mathrm{n}}(T)dT\right)^2}{\left(\sqrt{\int_{T_c}^{T_h} k_{\mathrm{p}}(T)dT \int_{T_c}^{T_{\mathrm{h}}} \rho_{\mathrm{p}}(T)dT} + \sqrt{\int_{T_c}^{T_{\mathrm{h}}} k_{\mathrm{n}}(T)dT \int_{T_c}^{T_h} \rho_{\mathrm{n}}(T)dT}\right)^2} \tag{19}$$

Since the output power is,

$$P_{\mathrm{out}} = \frac{V_{\mathrm{oc}}^2}{R} \frac{m}{(1+m)^2} \tag{20}$$

with,

$$V_{\mathrm{oc}} = \int_{T_c}^{T_h} S_{\mathrm{p}}(T)dT - \int_{T_c}^{T_h} S_{\mathrm{n}}(T)dT \tag{21}$$

from Equations (14), (20), and (21) the maximum efficiency is obtained [33, 34, 49],

$$\eta_{\mathrm{opt}} = \frac{\sqrt{1 + [Z]^{*}_{\mathrm{eng}} T_{\mathrm{h}} \alpha_1} - 1}{\alpha_0 \sqrt{1 + [Z]^{*}_{\mathrm{eng}} T_{\mathrm{h}} \alpha_1} + \alpha_2} \tag{22}$$

for $m = m_{\mathrm{opt}}$.

$$m_{\mathrm{opt}} = \sqrt{1 + [Z]^{*}_{\mathrm{eng}} T_{\mathrm{h}} \alpha_1} \tag{23}$$

The expressions of the coefficients α_{i} in Equation (22) and Equation (23) are reported in Equation (C.3). In particular, the maximum power output (and also the maximum efficiency, in this case [38]) is obtained if the following relation holds for the ratio β_{e} between the leg cross sectional areas $A_{\mathrm{n,p}}$ and the lengths $L_{\mathrm{n,p}}$.

$$\beta_{\mathrm{e}} = \frac{A_{\mathrm{n}} L_{\mathrm{p}}}{A_{\mathrm{p}} L_{\mathrm{n}}} = \sqrt{\frac{\int_{T_{\mathrm{c}}}^{T_{\mathrm{h}}} \rho_{\mathrm{n}}(T)dT \int_{T_{\mathrm{c}}}^{T_{\mathrm{h}}} k_{\mathrm{p}}(T)dT}{\int_{T_{\mathrm{c}}}^{T_{\mathrm{h}}} \rho_{\mathrm{p}}(T)dT \int_{T_{\mathrm{c}}}^{T_{\mathrm{h}}} k_{\mathrm{n}}(T)dT}} \tag{24}$$

Herefrom we assume $L_{\mathrm{n}} = L_{\mathrm{p}} = L$.

4. Test of model

Primarily, in order to test the reliability of the model we compared it with some experimental data extracted by literature. In particular, we used the results reported in [12] where a STEG configuration compatible with our model was experimented.

The efficiencies of a $\mathrm{Bi_2Te_3}$ STEG at various thermal concentrations (i.e. fill factors) were measured there by the authors for two different irradiances of 1000 W/m^2 and 1500 W/m^2. Moreover, the efficiencies for variable irradiances with two different thermal concentrations equal to 168 and 299 were measured too. We highlight that the materials used in those experiments are the same used here for our computations, where we also took into account the temperature dependence of thermoelectric characteristics of said materials. Using the parameters of system reported in [12, 13] we computed the indoor performances of that STEG obtaining the results reported in Figure 3 together with the experimental points. As can be noted the agreement obtained is rather good especially as regarding efficiency as function of thermal concentration.

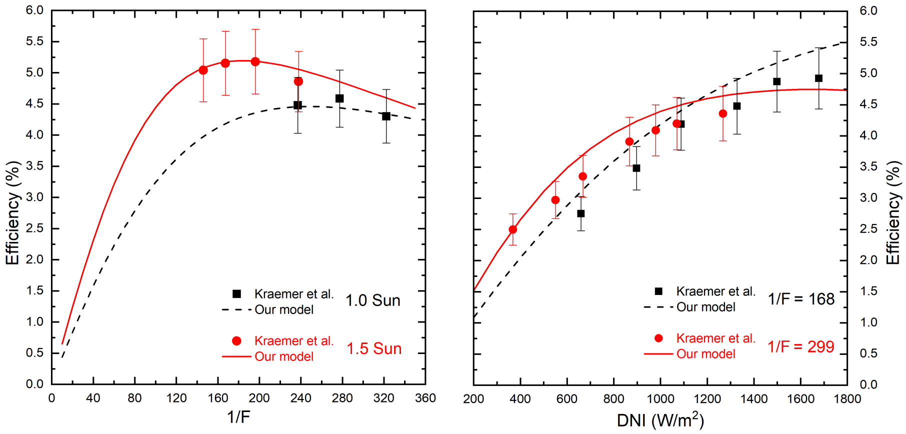

Figure 3: (left) Efficiency (cf. Equation (6)) as function of the thermal concentration 1/F for Bi_2Te_3 device of [12] with solar direct normal irradiance DNI of 1000 W/m^2 in black and 1500 W/m^2 in red. (right) Efficiency (cf. Equation (6)) as function of direct normal irradiance DNI for the Bi_2Te_3 device of [12] with thermal concentration of 168 in black and 299 in red.

Parameter	Symbol	Value	Units	Ref.
Enclosure transmission coefficient (Glass)	τ_{enc}	0.94	–	[12, 50, 51]
Emissivity of enclosure (AR coated glass)	ϵ_{enc}	0.1	–	[50–52]
Absorbance of SSA (Solar Selective Absorber)	α_{ssa}	0.95	–	[12, 51, 53]
Emissivity of SSA	α_{ssa}	0.05	–	[12, 51, 53]
Emissivity of metal contact (Cu)	ϵ_{Cu}	0.07	–	
Thermal conductivity of metal contact (Cu)	k_{Cu}	386	W/mK	
Thickness of metal contact (Cu)	d_{Cu}	25.4	μm	[54]
Thermal conductivity of alumina substrate	$k_{\text{Al}_2\text{O}_3}$	35.3	W/mK	
Thickness of alumina substrate	$d_{\text{Al}_2\text{O}_3}$	700	μm	[54]
CPC reflectance	ρ_{cpc}	0.95	–	[43]
heat sink thermal exchange coefficient	U	200	W/m^{2}K	
Ambient temperature	T_{a}	20	°C	[55]
Wind velocity	v	2	m/s	[55]

Table 1: List of parameter used in this work along with their exemplar values.

5. Computational procedures

In all the computations reported in this section we set $C_{\text{opt}} = 4$, a choice that implies a CPC acceptance angle of about 15°, requiring at most seasonal tracking adjustments for east-west orientation instead of a full tracking system. This reduces all costs related to the Balance Of System and the maintenance needs as well [56].

5.1. *Impact of the ambient conditions*

Ambient conditions may play a relevant role on the final system efficiency. We chose to use the Concentration Standard Operations Conditions (CSOC) for PV applications [55] to set the simulated ambient conditions. Therefore, the ambient temperature T_a was set to 20 °C and the wind velocity to 2 m/s. Specifically, the direct normal irradiance DNI is set to 900 $\mathrm{W/m^2}$ with no correction for a single-axis sun-tracker, assuming that the trough-like 2D-CPC was east-west oriented. Concerning solar irradiation we also considered DNIs of 400, 600 and 800 $\mathrm{W/m^2}$ to evaluate the impact of reduced irradiance on the conversion efficiency. The ambient temperature T_a was kept fixed, even though this parameter should be generally related to DNI. This was in agreement with the conclusion of previous works showing that the ambient temperature has a lesser impact than irradiance on the efficiency [44, 45]. The effect of the wind velocity on the system efficiency was computed using the well–known empirical equation [57],

$$h = (2.8\,\mathrm{W/m^2K}) + (3.0\,\mathrm{J/m^3K})v \tag{25}$$

which sets the convective heat loss coefficient h at the encapsulation top surface as a function of the wind velocity v. Anti-reflection and IR low emissivity coatings were assumed for both the inner and outer walls of the glass tube [50, 51].

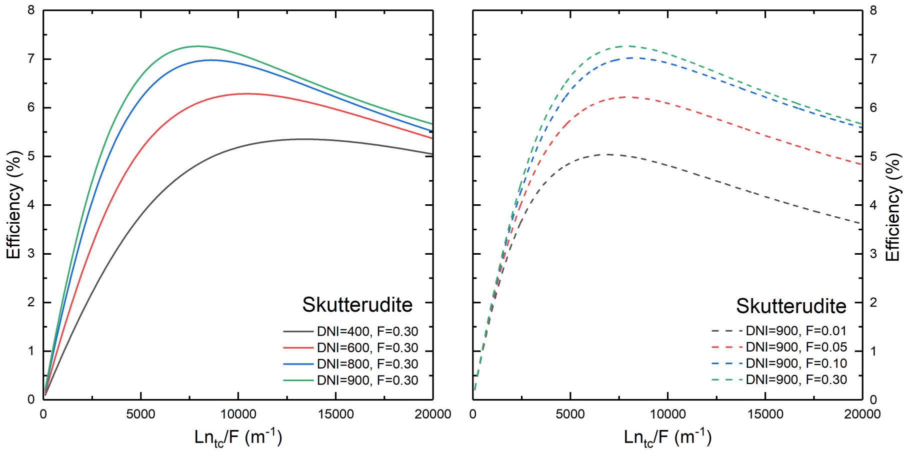

Figure 4: Efficiency (cf. Equation (6)) as function of the characteristic geometrical ratio r for skutterudite devices. Solar direct normal irradiance DNI between 400 $\mathrm{W/m^2}$ and 900 $\mathrm{W/m^2}$ (left) and fill factor between 0.01 and 0.3 were assumed (right). The spreading-constriction resistance and the alumina-copper substrates resistances were considered.

5.2. *Iterative solution and TEG optimization*

In general, the total efficiency of the TEG depends explicitly upon r, DNI and F, but not on n_{tc} directly. This provides an additional degree of freedom in the system design as the overall efficiency remains unchanged while changing n_{tc}, L and A, provided that the Ln_{tc}/A ratio remains constant. In particular, efficiency has a maximum over r. As an example Figure 4 reports the efficiencies as a function of r for variable DNIs and F values and for TEGs based on skutterudites.

The optimum layout can be searched for any desired combination of material, geometry and ambient parameters. Thus, for a given ambient condition, we could proceed to a simultaneous optimization of the TEG layout and the material characteristics. In fact, the leg geometry influences the TEG efficiency through the change of the material characteristics, which are dealt with as free parameters in our model. A maximum exists because the total efficiency is obtained as the product of the opto-thermal efficiency and of the pertinent TEG efficiency (Equation (6)).

The larger is r (i.e. $L/(A_n + A_p)$), the higher is the thermal resistance of the TCs, the temperature of the hot side, and the thermal gradient as well. Therefore, the efficiency grows with the temperature because of the latter component. However, if the temperature keeps increasing the radiative losses raise rapidly and soon prevails, so that the efficiency begins decreasing. The value of r from which the radiative losses prevail decreases with the DNI for any fixed fill factor F (Figure 4, left). In the right part of Figure 4, some typical trends at fixed DNIs are reported.

Based on the latter results we computed the maximum efficiency as a function of the fill factor F with DNIs from 400 $\mathrm{W/m^2}$ to 900 $\mathrm{W/m^2}$. The impact of the DNI depends on the materials, through the temperature dependence of the materials properties and, therefore, of the Thomson, Peltier and Joule effects. Such impact depends also on the geometry through the ratio $L/(A_n + A_p)$. Therefore, an optimal coupling between the ratio r, the materials properties, and the fill factor exists for any given DNI. In other words, the optimal combination material-geometry must be determined simultaneously for any given value of the opto-thermal concentration, of the environmental conditions and of the solar irradiance. Each maximum (for any assigned material and DNI) occurs at a specific value of r, which is a very weak function of F. Therefore with the aid of Equation (3) one may obtain the optimal value of Ln_{tc} at maximum efficiency as a function of F.

6. Results and discussion

We compared the performance of seven devices based on the materials listed in the Table 2. We studied a system configuration with low optical, high thermal concentration [12, 44, 45]. The ultimate aim was to optimize materials cost and conversion efficiency, then reducing the LCOE (Levelized Cost Of Energy) [19, 61, 62]. This approach is also useful in view of thermoelectric-thermal and/or PV cogeneration [14, 19, 38], since the system may be easily coupled to a thermal cogeneration system or a PV converter, so all the general conclusions of this work are also relevant for hybrid solar applications.

Short name	n-Material	p-Material	Ref.	$T_{\max}$ (°C)
BiTe	n-Bi_2Te_3	p-Bi_2Te_3	[58, 59]	300
PbTe	n-PbTe	p-PbTe	[60]	500
PbTe-PbSe	n-PbSe	p-PbTe	[1, 2]	500
SKU	n-$Ba_{0.06}La_{0.05}Yb_{0.04}Co_4Sb_{12}$	p-$Ce_{0.45}Nd_{0.45}Fe_{3.5}Co_{0.5}Sb_{12}$	[3, 4]	550
SiGe	n-SiGe	p-SiGe	[5, 6]	900
PbTe-SrTe	n-$PbTe_{1-x}I_x$	p-PbTe-SrTe	[7, 8]	500
HH	n-$Hf_{0.25}Zr_{0.75}NiSn_{0.99}Sb_{0.01}$	p-$Hf_{0.19}Zr_{0.76}Ti_{0.05}CoSb_{0.8}Sn_{0.2}$	[9, 10]	700

Table 2: Thermoelectric materials used in the computations reported in this work. $T_{\max}$ indicates the highest temperature at which each couple may be safely used.

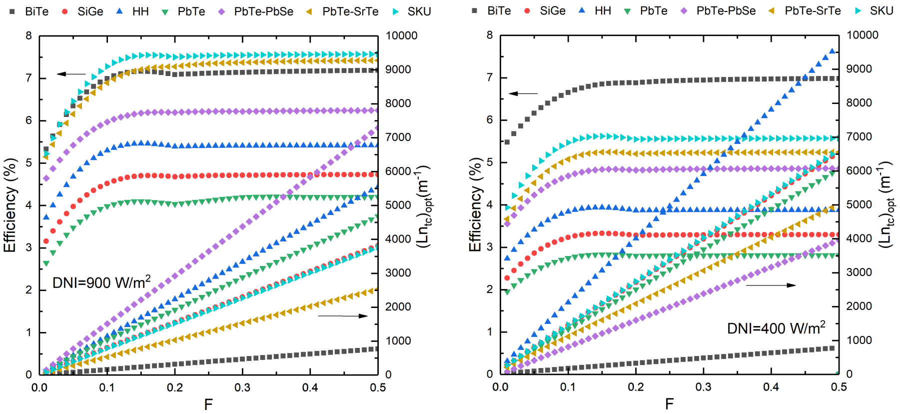

Figure 5: Efficiency (cf. Equation (6)) and $L \cdot n_{tc}$ as a function of the fill factor F for all materials considered in this work (Table 2). DNI was set to 400 W/m^2 and 900 W/m^2.

6.1. *Vacuum filling*

The results of the optimization procedure for DNIs of 400 W/m^2 (right) and 900 W/m^2 (left) under vacuum filling are reported in Figure 5.

The general trend of the curves can be easily understood. At first we note that the shunt losses are proportional to $A_{\mathrm{sh}}(F, C_{\mathrm{geo}})$ (cf. Equation (A.5)) so that, if $A_{\mathrm{sh}}(F, C_{\mathrm{geo}})$ and all the thermal resistances of the TEG, except those of the legs, are negligible, then the temperature profiles of the TCs are essentially determined by the ratio $L/(A_n+A_p) = r$. In such a case, the maximum efficiencies depend on F only by means of r and this is quite clearly our case for fill factors greater than 0.2 (see Figure 5). As result r essentially characterizes the STEG efficiency.

In any case, $(Ln_{tc})_{opt}$ depends on F linearly with very good approximation for the TEGs in vacuum conditions. Instead, for TEGs with low thermal conductivity filler and with $F < 0.2$ the shunt losses are important and $(Ln_{tc})_{opt}$ is no longer linear with F (Figure 7). However, starting from a sufficiently low fill factor, the thickness of substrates and metal contacts, and their resistances, are comparable with those of the legs. As a result, the efficiencies rapidly decrease with F. In particular cases, an acceptable efficiency reduction could be compensated by significant reductions of the materials cost. This is an important conclusion and must be carefully evaluated in order to reduce the LCOE (Levelized Cost Of Energy) if the material cost is preponderant.

The impact of the DNI depends on the materials. The results show that for DNI = 900 W/m^2 skutterutides, the nPbSe-pPbTe pair and Bi_2Te_3 have efficiencies higher than $\simeq 7\%$ in the studied range of thermal concentrations. What is even more remarkable, however, is that Bi_2Te_3 efficiency decreases of less than $\simeq$ 2.5% from DNI = 900 W/m^2 to DNI = 400 W/m^2, whereas for the other two materials it decreases of $\simeq$ 30%. This is a key point from the energy production point of view, due to seasonally and daily variations of the DNI. These best performances of Bi_2Te_3 in our conditions are principally due to the cumulative effect of the higher efficiencies at lower temperatures (see Appendix C).

Another major advantage of Bi_2Te_3, making it the best material in the current scenario, are the relatively low values of the Ln_{tc}/F ratio needed to obtain the highest efficiencies for each fill factor. For Bi_2Te_3 the optimal Ln_{tc} is well below 1000 m^{-1} for fill factors between 0.1 and 0.2. This makes much easier to practically implement the low values of optimal lengths required for any given n_{tc}. Therefore, Bi_2Te_3 enables simultaneously optimized geometries and annual energy productions at all solar irradiation levels, with the temperature of the hot side of the TEG for Bi_2Te_3 fully within the range of safe usability of the material. This is not the case for all materials, a factor that would force them to be operated under sub-optimal conditions.

Finally, Figure 6 reports the curves of the hot-side temperatures and the ΔT at the edges of the legs as functions of the fill factor F. Note that higher ΔT and T_{h} not necessary correspond to higher efficiencies. Thus, concentration does not avail all materials.

6.2. Non-vacuum filling

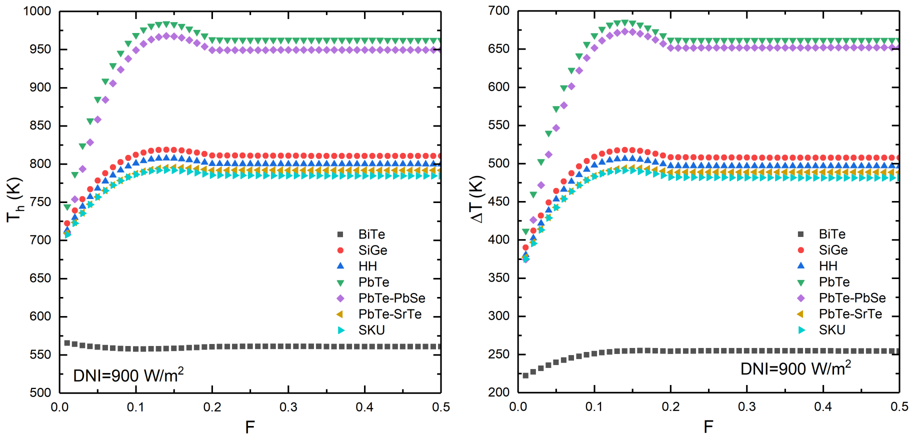

Figure 6: Hot-side temperature (left) and temperature difference (right) as a function of the fill factor F for all materials considered in this work (Table 2). DNI was set to 900 W/m^2.

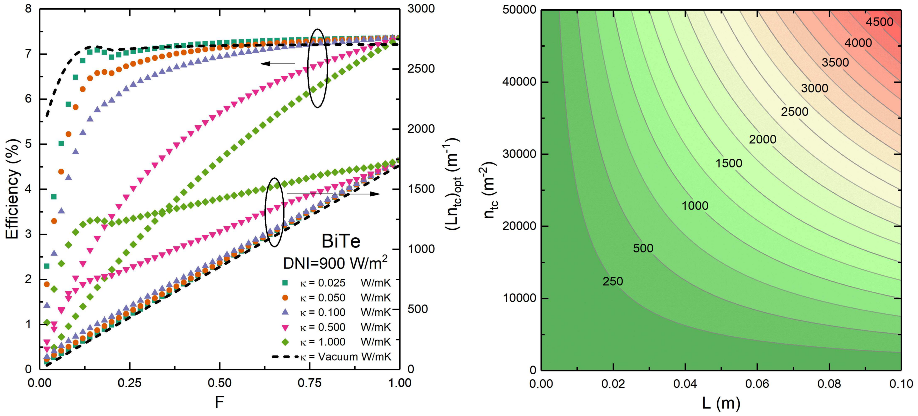

Figure 7: (Left) Efficiency (cf. Equation (6)) and optimal product Ln_{tc} as a function of the fill factor F for $\mathrm{Bi_2Te_3}$ devices. Filler materials with thermal conductivities between 0.025 W/mK and 1 W/mK were considered. Both the Thomson effect and a variable Joule weights were used. (Right) A contour plot of Ln_{tc} as a function of leg lengths and TC densities.

We also simulated TEGs with suitable materials filling the leg gap. Spanning thermal conductivities k_{filler} between 0.025 W/mK of silica aerogel, or foam glass and plastics [63, 64], and 0.5 W/mK of polymers [63], we found (Figure 7, left) that for conductivity as low as 0.025-0.05 W/mK fillers perform better than vacuum, as they suppress the radiative heat exchange.

It must be also considered that suitable fillers could provide mechanical support in the case of high leg aspect ratios. As an example, for $F \simeq 0.12$ a $\mathrm{Bi_2Te_3}$ TEG have an efficiency greater than 7% and an optimal $Ln_{\mathrm{tc}} \simeq 250\ \mathrm{m}^{-1}$. Thus, Figure 7, right shows that a TEG with a TC density of $1\ \mathrm{cm}^{-2}$ requires leg lengths of about 2 cm; as an alternative, lengths of about 1 cm are needed for $n_{\mathrm{tc}} = 3\ \mathrm{cm}^{-2}$.

Finally, we already noted that the ratios $L/A_{n,p}$ univocally determine the temperature profiles in the legs (Equations (17), (18) and (24)) once materials, fill factor, and incident radiation are set. This is true if edge effects on the thermal fluxes can be neglected. In fact, the convection heat exchanges in a closed chamber are in general not scale invariant, but they do not occur into the vacuum tube embedding the TEG devices. On the contrary, the radiative exchanges between the exterior of the glass tube and the ambient through the CPC walls are scale invariant because the exchange factor is equal to one (cf. Equation (B.2)). As a result, scaling up or down the system without varying F also leaves unchanged the efficiency of the TEG unit. This is an important point not only to generalize the results of the modelling but also from a practical point of view. For any given concentration, in fact, the larger is the linear entering aperture of the CPC, the larger is its height and its exit aperture [48]. This obviously makes the device implementation more difficult and increases costs for larger exit apertures. In particular, it is always possible (and convenient) to reduce a generic 2D-CPC to an equivalent CPC trough with exit aperture equal to $\sqrt{1/n_{\mathrm{tc}}}$. Thus, any analyzed configuration is representative of an entire class of thermoelectric converters.

This is a key point of our approach. Often, in literature one or more geometrical parameters (thickness, length, etc..) of TEGs and legs are arbitrarily kept fixed, and the maximum efficiency is searched by varying the remaining parameters. This implicitly neglects the fact that the maximum of a function of several variables must be searched by setting to zero its total derivative, not some partial derivatives. As a result, if one disregards the role of materials parameters (keeping them fixed), the device layout one obtains may not be optimal for other materials. Likewise, fixing an intrinsically variable quantity as the DNI leads to a selection of TE materials and device geometry that may not be optimal for different values of the DNI. This brings to one of the most important point of this paper: any search for an optimal material and device layout is improper and misleading. Instead, one must consider that (1) the optimal efficiency of a solar harvester globally depends on TE materials properties, device layout (including coupling parameters such as C_{opt}), and the DNI; and (2) that the variability of the DNI may significantly impact the optimization of the harvester (materials and layout). Therefore, the choice of the ”best system” must unavoidably be thought as a compromise that accounts for such variability, namely selecting the system that, on the average, better fulfills local solar irradiance. This explains why our conclusions about the dependence of a Bi_2Te_3-based thermoelectric system upon n_{tc} differ from those obtained by Lamba *et al.* [65] by optimizing the efficiency *after* setting the leg aspect ratio and n_{tc}. Obviously the described procedure can be applied for any other desired geometrical concentration or ambient conditions.

7. Conclusions

In this work, theoretical predictions of power production of a solar thermoelectric generator are reported using a model which was validated by comparison with experimental literature data. The system considered is made of a compound parabolic concentrator concentrating solar radiation with a fixed 4× ratio on a thermoelectric generator covered with a state-of-the-art solar selective absorber and placed in an evacuated glass tube.

The efficiencies of the devices were computed for various solar irradiation levels and TEG materials and designs. In particular the irradiance was varied between 400 and 900 W/m^2. To make the model more accurate the variation with temperature of the thermoelectric characteristics of the materials considered were taken into account along with the Thomson effect and a computed Joule weight. In addition, evacuated TEGs were compared to TEGs filled with thermal insulators.

We found that the best efficiencies were reached for a DNI of 900 W/m^2 with skutterudites, which were found capable of an overall efficiency of about 7.5 % with a filling factor of 0.1. However, the system temperature and the final efficiency were found to be strongly dependent on the solar irradiation level, with the efficiency dropping to about 5.5% at a DNI of 400 W/m^2. Instead, Bi_2Te_3-based devices showed good efficiencies of about 7 % for all DNIs. Therefore, their average yearly performances are expected to be better than those of any other studied material. In addition, the optimal aspect ratios of legs for Bi_2Te_3 was found simpler to implement.

Finally, the comparison between evacuated and filled TEGs showed similar efficiencies when the filler thermal conductivity is < 0.1 W/mK. This opens factual possibilities for non-evacuated STEGs, which will simplify their manufacturability.

Acknowledgements

Part of this work was financed by the Region Puglia (Bari, Italy) within the program “Reti di laboratori pubblici di ricerca”– project ZERO (code 55).

B. L. has received funding from the European Union’s Horizon 2020 research and innovation program under the Marie Skłodowska-Curie grant agreement No. 745304.

Appendix A. Spreading/constriction, metallic contact and substrate thermal resistances

The concept of spreading/constriction resistances are common and useful [12, 46, 66] because they allow to approximate as uniform the temperature distributions at the interfaces between TCs and the absorbing and cooling substrates (rear-cooled and front-heated substrates) [66]. Thus, if the lateral surface of TEG module and the horizontal heat flux through it can be neglected the problem can be dealt with as 1D (negligible edge effects). This is possible also because, as can be easily proved, the temperature profiles along the legs are approximately linear [33].

As regarding the constriction thermal conductance K_{con} at the TC hot side and the spreading thermal conductance K_{sp} at the TC cold side, we followed the approach suggested by Vermeersch et a. [66]. More precisely, for the simmetry of the TEG device we have $K_{\mathrm{con}} = K_{\mathrm{sp}} = K_{\mathrm{sc}}$ with.

$$K_{\mathrm{sc}} = \frac{k_{\mathrm{x}} F_{\mathrm{teg}} A (1 + 2\lambda \tan(\phi))}{d_{\mathrm{x}}} \tag{A.1}$$

Here

$$\phi = \begin{cases} 5.86 \log \lambda + 40.4 & 0.0011 < \lambda \leq 1 \\ 46.45 - 6.048 \lambda^{-0.969} & \lambda \geq 1 \end{cases} \tag{A.2}$$

is the angle of spreading/constriction [67] which is ideally formed by heat flowing into/out of the leg (heat source) through the substrate of thickness d_{x} and/or the copper sheet and.

$$\lambda = \frac{d_{\mathrm{x}}}{\sqrt{F_{\mathrm{teg}} A}} \tag{A.3}$$

Practically we should use twice Equation (A.1) to calculate the spreading/constriction conductance between the cross-section of the TC legs and copper foil and then between copper and the alumina substrate. In any case, however, copper sheet is assumed to be much thinner than the alumina substrate (see Equation (A.1) and Table 1) so that its heat spreading/constriction effect can be neglected ($\phi \cong 0$) and the resistance contribution of the metallic sheet can be reduced to that of a portion of material of area equal to the leg cross-section, $F_{\mathrm{teg}}A$, and thickness d_{Cu}. Therefore, for the total conductance $K_{\mathrm{sub+Cu}}$ at the hot and cold-side TEG-substrate contacts we had.

$$K_{\mathrm{sub+Cu}} = \frac{1}{\dfrac{d_{\mathrm{Cu}}}{k_{\mathrm{Cu}}F_{\mathrm{teg}}A} + \dfrac{d_{\mathrm{Al_2O_3}}}{k_{\mathrm{Al_2O_3}}F_{\mathrm{teg}}A(1+2\lambda\tan(\phi))}} \tag{A.4}$$

When the radiative or the conductive heat shunted out of the legs are considered, a suitable area $\mathrm{A}_{\mathrm{sh}}(F_{\mathrm{teg}}, C_{\mathrm{geo}})$ must be used in equations (7) and (8). Namely, with reference one TC of area $A = S/C_{\mathrm{geo}}$, the area can be written as.

$$\mathrm{A}_{\mathrm{sh}}(F_{\mathrm{teg}}, C_{\mathrm{geo}}) = \frac{S(1-F_{\mathrm{teg}})}{C_{\mathrm{geo}}} - \\ - 4d_{\mathrm{Al_2O_3}}\left(\sqrt{F_{\mathrm{teg}}A}\tan(\phi) + F_{\mathrm{teg}}A\tan(\phi)^2\right) \tag{A.5}$$

The second term in the right-hand side is the additional contour area around the cross-section of legs $F_{\mathrm{teg}}A$ which is involved into heat spreading/constriction [67].

Finally, we defined the following thermal conductances to complete thermal modelling of entire system:

$$K_{\mathrm{rad,SSA}}(T_{\mathrm{s}}, T_{\mathrm{enc}}) = \sigma\epsilon_{\mathrm{eq,SSA}}\,\mathrm{A}(C_{\mathrm{geo}})(T_{\mathrm{s}} + T_{\mathrm{enc}})(T_{\mathrm{s}}^2 + T_{\mathrm{enc}}^2) \tag{A.6}$$

$$K_{\mathrm{rad,TEG}}(T_{\mathrm{h}}, T_{\mathrm{c}}) = \sigma\epsilon_{\mathrm{eq,sub}}\,\mathrm{A}_{\mathrm{sh}}(F_{\mathrm{teg}}, C_{\mathrm{geo}})(T_{\mathrm{h}} + T_{\mathrm{c}})(T_{\mathrm{h}}^2 + T_{\mathrm{c}}^2) \tag{A.7}$$

$$K_{\mathrm{rad,enc}}(T_{\mathrm{enc}}, T_{\mathrm{a}}) = \sigma\epsilon_{\mathrm{enc}}\,\mathrm{A}_{\mathrm{enc}}(C_{\mathrm{geo}})(T_{\mathrm{enc}} + T_{\mathrm{a}})(T_{\mathrm{enc}}^2 + T_{\mathrm{a}}^2) \tag{A.8}$$

where, σ is the Stefan-Boltzmann constant; $\epsilon_{\mathrm{eq,SSA}}$ is the equivalent emissivity of the SSA absorber of area A facing the internal face of the front enclosure with area $A_{\mathrm{enc}} = (\pi/2)A$, here assumed as a glass cylindrical tube kept in vacuum embedding the SSA (see Fig. 1); $\epsilon_{\mathrm{eq,sub}}$ is the equivalent emissivity of the facing hot-side and cold-side plates of the TEG; ϵ_{enc} is the external emissivity of the evacuated tube; h is the convective heat transfer coefficient.

Appendix B. Equivalent emissivities of the system

The heat transferred by radiation from a surface of area A_1 to another one of area A_2 , with temperatures respectively T_1 and T_2, can be expressed as [68, Chap.13]

$$q_{1\to2} = \frac{\sigma(T_1^4 - T_2^4)}{\dfrac{1-\epsilon_1}{A_1\epsilon_1} + \dfrac{1}{A_1F_{1\to2}} + \dfrac{1-\epsilon_2}{A_2\epsilon_2}} \tag{B.1}$$

where $F_{1\to2}$ is the View Factor between the two surfaces [68, Chap.13]. In particular, in a two-surface enclosure like that formed by SSA and the internal surface of the evacuated tube, we had $A_1 = A$, $A_2 = A_{\text{enc}} = (\pi/2)A$ and $F_{1\to 2} = 1$, so that a suitable equivalent emissivity $\epsilon_{\text{eq,SSA}}$ may be introduced,

$$\epsilon_{\text{eq,SSA}} = \frac{1}{\dfrac{1-\epsilon_{\text{SSA}}}{\epsilon_{\text{SSA}}} + 1 + \dfrac{1-\epsilon_{\text{enc}}}{(\pi/2)\epsilon_{\text{enc}}}} \tag{B.2}$$

with ϵ_{SSA} and ϵ_{enc} are the emissivities of the selective absorber and tubular enclosure respectively. By means of definitions (B.2) and (A.6) the Stefan-Boltzmann expression of the exchanged power between the two surfaces can be recast as a Fourier-like term in the left-hand side of equation (9).

Actually, as shown by A. Rabl [41], to correctly describe the heat radiation transfer through a CPC the useful concept of Exchange View Factors must be introduced.

In particular, in a CPC all the radiation hemispherically emitted by the absorber intercepts the front aperture within the acceptance angle [40], and then a View Factor equal to one can be assumed between absorber and the ambient. Then, applying Eq. (B.1) and assuming the ambient as a black-body one obtains an equivalent emissivity exactly equal to ϵ_{enc}.

Finally, for the facing hot and cold-side plates in TEG device, we obtained,

$$\epsilon_{\text{eq,sub}} = \frac{1}{\dfrac{1-\epsilon_{\text{Cu}}}{\epsilon_{\text{Cu}}} + \dfrac{1}{F_{\text{h}\to\text{c}}} + \dfrac{1-\epsilon_{\text{Cu}}}{\epsilon_{\text{Cu}}}} \tag{B.3}$$

with ϵ_{Cu} the emissivity of the metal contact and where for the parallel plates view factor $F_{\text{h}\to\text{c}}$ we used the expression [68, Chap.13],

$$F_{\text{h}\to\text{c}} = \frac{2}{\pi\bar{a}^2}\left\{\ln\sqrt{\frac{(1+\bar{a}^2)^2}{1+2\,\bar{a}^2}} + \right. \\ \left. +2\,\bar{a}\sqrt{(1+\bar{a}^2)}\arctan\frac{\bar{a}}{\sqrt{(1+\bar{a}^2)}} - 2\,\bar{a}\arctan\bar{a}\right\} \tag{B.4}$$

with $\bar{a} = \sqrt{F_{\text{teg}}A}/L$ is the side length of the squared associated to one TC normalized by the leg length. Here, we neglected the area covered by legs and the related shadow effect because, in general, we have small fill factors at the optimum working points.

Appendix C. Weight factors and auxilary coefficients of Joule and Thomson effects

Kim et al. [33, 49] and Liu et al. [69] introduced and used the following coefficients to weight the Joule and Thomson effects.

$$W_{\text{J,p-n}} = \frac{\int_{T_c}^{T_h}\int_{T}^{T_h}\rho_{\text{p-n}}dT}{\Delta T\int_{T_c}^{T_h}\rho_{\text{p-n}}dT} \tag{C.1}$$

$$W_{\mathrm{T,p-n}} = \frac{\int_{T_c}^{T_h}\int_{T}^{T_h} \tau_{\mathrm{p-n}} dT}{\Delta T \int_{T_c}^{T_h} \tau_{\mathrm{p-n}} dT} \tag{C.2}$$

These coefficients naturally emerge by the double integration of Domenicali equation Equation (13) in space variable x followed from a variable exchange and with the assumption $\frac{dx}{dT} \simeq -\frac{L_{\mathrm{p,n}}}{\Delta T}$. Regarding the last condition it was observed that empirical evidence shows that the inverse function x(T) exists for a TEG, even though a rigorous proof of this is still missing [70, 71]. Furthermore, the temperature gradients result to be linear with good approximation for the cases we studied here [33]. It is possible to test this fact also by solving directly and *a posteriori* the Domenicali equation using as edge temperatures those obtained by the cumulative modelling.

To calculate the optimal efficiency of Equation (22) the following coefficients must be used,

$$\alpha_{\mathrm{i}} = \frac{\left(S_{\mathrm{p}}(T_{\mathrm{h}}) - S_{\mathrm{n}}(T_{\mathrm{h}})\right)\Delta T}{V_{\mathrm{oc}}} - \frac{\left(W_{\mathrm{T,p}} \int_{T_c}^{T_h} \tau_{\mathrm{p}}(T) dT - W_{\mathrm{T,n}} \int_{T_c}^{T_h} \tau_{\mathrm{n}}(T) dT\right)}{V_{\mathrm{oc}}}\eta_{\mathrm{c}} - i\frac{\left(W_{\mathrm{J,p}} \int_{T_c}^{T_h} \rho_{\mathrm{p}}(T) dT + W_{\mathrm{J,n}} \int_{T_c}^{T_h} \rho_{\mathrm{n}}(T) dT\right)}{R}\eta_{\mathrm{c}} \tag{C.3}$$

with i=0, 1, 2.

References

[1] Q. Zhang, E. K. Chere, K. McEnaney, M. Yao, F. Cao, Y. Ni, S. Chen, C. Opeil, G. Chen, Z. Ren, Enhancement of thermoelectric performance of n-Type PbSe by Cr doping with optimized carrier concentration, Advanced Energy Materials 5 (8) (2015) 1–8. `doi:10.1002/aenm.201401977`.

[2] Q. Zhang, F. Cao, W. Liu, K. Lukas, B. Yu, S. Chen, C. Opeil, D. Broido, G. Chen, Z. Ren, Heavy doping and band engineering by potassium to improve the thermoelectric figure of merit in p-type PbTe, PbSe, and PbTe 1- ySe y, Journal of the American Chemical Society 134 (24) (2012) 10031–10038. `doi:10.1021/ja301245b`.

[3] X. Shi, J. Yang, J. R. Salvador, M. Chi, J. Y. Cho, H. Wang, S. Bai, J. Yang, W. Zhang, L. Chen, Multiple-filled skutterudites: High thermoelectric figure of merit through separately optimizing electrical and thermal transports, Journal of the American Chemical Society 133 (20) (2011) 7837–7846. `doi:10.1021/ja111199y`.

[4] Q. Jie, H. Wang, W. Liu, H. Wang, G. Chen, Z. Ren, Fast phase formation of double-filled p-type skutterudites by ball-milling and hot-pressing., Physical chemistry chemical physics : PCCP 15 (2013) 6809–16. `doi:10.1039/c3cp50327e`.

[5] G. Joshi, H. Lee, Y. Lan, X. Wang, G. Zhu, D. Wang, R. W. Gould, D. C. Cuff, M. Y. Tang, M. S. Dresselhaus, G. Chen, Z. Ren, Enhanced thermoelectric figure-of-merit in nanostructured p-type silicon germanium bulk alloys, Nano Letters 8 (12) (2008) 4670–4674, pMID: 18973391. `arXiv:http://dx.doi.org/10.1021/nl8026795`, `doi:10.1021/nl8026795`.

[6] X. W. Wang, H. Lee, Y. C. Lan, G. H. Zhu, G. Joshi, D. Z. Wang, J. Yang, A. J. Muto, M. Y. Tang, J. Klatsky, S. Song, M. S. Dresselhaus, G. Chen, Z. F. Ren, Enhanced thermoelectric figure of merit in nanostructured n -type silicon germanium bulk alloy, Applied Physics Letters 93 (19) (2008) 1–4. `doi:10.1063/1.3027060`.

[7] K. Biswas, J. He, I. D. Blum, C.-I. Wu, T. P. Hogan, D. N. Seidman, V. P. Dravid, M. G. Kanatzidis, High-performance bulk thermoelectrics with all-scale hierarchical architectures., Nature 489 (7416) (2012) 414–8. `doi:10.1038/nature11439`.

[8] A. D. LaLonde, Y. Pei, G. J. Snyder, Reevaluation of pbte1-xix as high performance n-type thermoelectric material, Energy Environ. Sci. 4 (2011) 2090–2096. `doi:10.1039/C1EE01314A`.

[9] S. Chen, K. C. Lukas, W. Liu, C. P. Opeil, G. Chen, Z. Ren, Effect of Hf concentration on thermoelectric properties of nanostructured n-type half-heusler materials HfxZr1-xNiSn 0.99Sb0.01, Advanced Energy Materials 3 (9) (2013) 1210–1214. `doi:10.1002/aenm.201300336`.

[10] R. He, H. S. Kim, Y. Lan, D. Wang, S. Chen, Z. Ren, Investigating the thermoelectric properties of p-type half-heusler hfx(zrti)1-xcosb0.8sn0.2 by reducing hf concentration for power generation, RSC Adv. 4 (2014) 64711–64716. doi:10.1039/C4RA14343D.

[11] M. Telkes, Solar thermoelectric generators, Journal of Applied Physics 25 (6) (1954) 765–777. doi:10.1063/1.1721728.

[12] D. Kraemer, B. Poudel, H.-P. Feng, J. C. Caylor, B. Yu, X. Yan, Y. Ma, X. Wang, D. Wang, A. Muto, K. McEnaney, M. Chiesa, Z. Ren, G. Chen, High-performance flat-panel solar thermoelectric generators with high thermal concentration, Nature materials 10 (7) (2011) 422–427.

[13] D. Kraemer, Q. Jie, K. McEnaney, F. Cao, W. Liu, L. A. Weinstein, J. Loomis, Z. Ren, G. Chen, Concentrating solar thermoelectric generators with a peak efficiency of 7.4%, Nature Energy 1 (11) (2016) 16153. doi:10.1038/nenergy.2016.153.

[14] K.-T. Park, S.-M. Shin, A. S. Tazebay, H.-D. Um, J.-Y. Jung, S.-W. Jee, M.-W. Oh, S.-D. Park, B. Yoo, C. Yu, J.-H. Lee, Lossless hybridization between photovoltaic and thermoelectric devices, Scientific Reports 3 (1) (2013) 2123. doi:10.1038/srep02123.

[15] O. Beeri, O. Rotem, E. Hazan, E. A. Katz, A. Braun, Y. Gelbstein, Hybrid photovoltaic-thermoelectric system for concentrated solar energy conversion: Experimental realization and modeling, Journal of Applied Physics 118 (11) (2015) 115104. arXiv:https://doi.org/10.1063/1.4931428, doi:10.1063/1.4931428.
URL https://doi.org/10.1063/1.4931428

[16] S. Shittu, G. Li, X. Zhao, X. Ma, Series of detail comparison and optimization of thermoelectric element geometry considering the pv effect, Renewable Energy 130 (2019) 930 – 942. doi:https://doi.org/10.1016/j.renene.2018.07.002.
URL http://www.sciencedirect.com/science/article/pii/S0960148118307870

[17] S. Lv, W. He, Z. Hu, M. Liu, M. Qin, S. Shen, W. Gong, High-performance terrestrial solar thermoelectric generators without optical concentration for residential and commercial rooftops, Energy Conversion and Management 196 (2019) 69–79. doi:10.1016/j.enconman.2019.05.089.

[18] D. L. Chubb, B. S. Good, A combined thermophotovoltaic-thermoelectric energy converter, Solar Energy 159 (2018) 760 – 767. doi:https://doi.org/10.1016/j.solener.2017.11.030.
URL http://www.sciencedirect.com/science/article/pii/S0038092X17310137

[19] P. Bermel, K. Yazawa, J. L. Gray, X. Xu, A. Shakouri, Hybrid strategies and technologies for full spectrum solar conversion, Energy Environ. Sci. (2016) 2776–2788`doi:10.1039/C6EE01386D`.

[20] D. Narducci, P. Bermel, B. Lorenzi, N. Wang, K. Yazawa, Hybrid and Fully Thermoelectric Solar Harvesting, Vol. 268 of Springer Series in Materials Science, Springer, 2018.

[21] G. Li, S. Shittu, T. M. Diallo, M. Yu, X. Zhao, J. Ji, A review of solar photovoltaic-thermoelectric hybrid system for electricity generation, Energy 158 (2018) 41 – 58. `doi:https://doi.org/10.1016/j.energy.2018.06.021`.
URL `http://www.sciencedirect.com/science/article/pii/S0360544218310740`

[22] K. Tappura, A numerical study on the design trade-offs of a thin-film thermoelectric generator for large-area applications, Renewable Energy 120 (2018) 78–87. `doi:10.1016/j.renene.2017.12.063`.
URL `https://doi.org/10.1016/j.renene.2017.12.063`

[23] L. A. Weinstein, K. McEnaney, G. Chen, Modeling of thin-film solar thermoelectric generators, Journal of Applied Physics 113 (2013) 164504.

[24] W. Zhu, Y. Deng, M. Gao, Y. Wang, Hierarchical Bi–Te based flexible thin-film solar thermoelectric generator with light sensing feature, Energy Conversion and Management 106 (2015) 1192–1200.

[25] K. McEnaney, D. Kraemer, Z. Ren, G. Chen, Modeling of concentrating solar thermoelectric generators, Journal of Applied Physics 110 (7) (2011) 074502. `arXiv:https://doi.org/10.1063/1.3642988`, `doi:10.1063/1.3642988`.
URL `https://doi.org/10.1063/1.3642988`

[26] D. Kraemer, K. McEnaney, M. Chiesa, G. Chen, Modeling and optimization of solar thermoelectric generators for terrestrial applications, Solar Energy 86 (5) (2012) 1338–1350. `doi:10.1016/j.solener.2012.01.025`.

[27] S. Su, J. Chen, Simulation investigation of high-efficiency solar thermoelectric generators with inhomogeneously doped nanomaterials, IEEE Transactions on Industrial Electronics 62 (6) (2015) 3569–3575.

[28] J. Xiao, T. Yang, P. Li, P. Zhai, Q. Zhang, Thermal design and management for performance optimization of solar thermoelectric generator, Applied Energy 93 (2012) 33–38.

[29] W. H. Chen, C. C. Wang, C. I. Hung, C. C. Yang, R. C. Juang, Modeling and simulation for the design of thermal-concentrated solar thermoelectric generator, Energy 64 (2014) 287–297. `doi:10.1016/j.energy.2013.10.073`.
URL `http://dx.doi.org/10.1016/j.energy.2013.10.073`

[30] F. S. Moraes, L. C. Santos, R. N. Alencar, Éric V. Sempels, J. C. S. V, F. J. Lesage, Solar thermoelectric generator performance relative to air speed, Energy Conversion and Management 99 (2015) 326 – 333. doi:https://doi.org/10.1016/j.enconman.2015.04.049.
URL http://www.sciencedirect.com/science/article/pii/S0196890415004033

[31] M. Ge, Z. Wang, L. Liu, J. Zhao, Y. Zhao, Performance analysis of a solar thermoelectric generation (STEG) system with spray cooling, Energy Conversion and Management 177 (October) (2018) 661–670. doi:10.1016/j.enconman.2018.10.016.
URL https://doi.org/10.1016/j.enconman.2018.10.016

[32] H. He, W. Liu, Y. Wu, M. Rong, P. Zhao, X. Tang, An approximate and efficient characterization method for temperature-dependent parameters of thermoelectric modules, Energy Conversion and Management 180 (2019) 584 – 597. doi:https://doi.org/10.1016/j.enconman.2018.11.002.
URL http://www.sciencedirect.com/science/article/pii/S019689041831238X

[33] H. S. Kim, W. Liu, G. Chen, C.-W. Chu, Z. Ren, Relationship between thermoelectric figure of merit and energy conversion efficiency., Proceedings of the National Academy of Sciences of the United States of America 112 (27) (2015) 8205–10. doi:10.1073/pnas.1510231112.

[34] H. S. Kim, W. Liu, Z. Ren, Efficiency and output power of thermoelectric module by taking into account corrected Joule and Thomson heat, Journal of Applied Physics 118 (11) (2015) 115103. doi:10.1063/1.4930869.

[35] E. Kanimba, Z. Tian, A new dimensionless number for thermoelectric generator performance, Applied Thermal Engineering 152 (2019) 858–864. doi:10.1016/j.applthermaleng.2019.02.093.

[36] Y. Wang, M. Zhang, Y. Tian, Z. Wu, J. Xing, Y. Li, J. Mao, J. Li, H. Xie, Influence of Thomson effect on efficiency of thermoelectric generator, International Journal of Heat and Mass Transfer 137 (2019) 1183–1190. doi:10.1016/j.ijheatmasstransfer.2019.03.155.

[37] K. Shanks, S. Senthilarasu, T. K. Mallick, Optics for concentrating photovoltaics: Trends, limits and opportunities for materials and design, Renewable and Sustainable Energy Reviews 60 (2016) 394–407. doi:10.1016/j.rser.2016.01.089.

[38] G. Chen, Theoretical efficiency of solar thermoelectric energy generators, Journal of Applied Physics 109 (10) (2011) 104908. doi:10.1063/1.3583182.

[39] N. ur Rehman, M. Uzair, M. A. Siddiqui, Optical analysis of a novel collector design for a solar concentrated thermoelectric generator, Solar Energy 167 (2018) 116 – 124. doi:https://doi.org/10.1016/j.solener.2018.03.087.

URL http://www.sciencedirect.com/science/article/pii/S0038092X18303438

[40] R. Winston, H. Hinterberger, Principles of Cylindrical Concentrators for Solar Energy, Solar Energy 16 (1974) 89.

[41] A. Rabl, Solar concentrators with maximal concentration for cylindrical absorbers., Applied optics 15 (7) (1976) 1871–1873. doi:10.1364/AO.15.001871.

[42] A. Rabl, R. Winston, Ideal concentrators for finite sources and restricted exit angles, Applied optics 15 (11) (1976) 2880–3. doi:10.1364/AO.15.002880.

[43] A. Rabl, N. Goodman, R. Winston, Practical design considerations for CPC solar collectors, Solar Energy 22 (1979) 373–381. doi:http://dx.doi.org/10.1016/0038-092X(79)90192-0.

[44] B. Lorenzi, G. Contento, V. Sabatelli, A. Rizzo, D. Narducci, Theoretical Analysis of Two Novel Hybrid Thermoelectric - Photovoltaic Systems Based on CZTS Solar Cells, J. Nanosci. Nanotechnol. 17 (2017) 1608–1615.

[45] G. Contento, B. Lorenzi, A. Rizzo, D. Narducci, Efficiency enhancement of a-Si and CZTS solar cells using different thermoelectric hybridization strategies, Energy 131 (2017) 230 – 238.

[46] K. Yazawa, A. Shakouri, Cost-Efficiency Trade-off and the Design of Thermoelectric Power Generators, Environmental Science & Technology 45 (17) (2011) 7548–7553.

[47] K. Yazawa, A. Shakouri, Exergy Analysis and Entropy Generation Minimization of Thermoelectric Waste Heat Recovery for Electronics, Proceedings of the ASME 2011 Pacific Rim Technical Conference and Photonic Systems (2011) 1–7doi:10.1115/IPACK2011-52191.

[48] A. Rabl, Optical and thermal properties of compound parabolic concentrators, Solar Energy 18 (6) (1976) 497–511. doi:10.1016/0038-092X(76)90069-4.

[49] H. S. Kim, W. Liu, Z. Ren, The bridge between the materials and devices of thermoelectric power generators, Energy Environ. Sci. (2017). doi:10.1039/C6EE02488B.

[50] H. L. Yang, L. Hao, J. N. Wang, Z. N. Zhang, X. P. Liu, L. J. Jiang, Self-Cleaning and Antireflective Films for All-Glass Evacuated Tube Solar Collectors, Energy Procedia 69 (2015) 226–232. doi:10.1016/j.egypro.2015.03.026.

[51] J. Wang, Z. Yin, J. Qi, G. Ma, X. Liu, Medium-temperature Solar Collectors with All-glass Solar Evacuated Tubes, Energy Procedia 70 (2015) 126–129. doi:10.1016/j.egypro.2015.02.107.

[52] Pilkington.com, Low-emissivity Glass, https://www.pilkington.com/en-gb/uk/householders/types-of-glass/energy-efficient-glass/low-emissivity-glass, accessed: 2018-12-11 (2018).

[53] S. Suman, M. K. Khan, M. Pathak, Performance enhancement of solar collectors - A review, Renewable and Sustainable Energy Reviews 49 (2015) 192–210. doi:10.1016/j.rser.2015.04.087.

[54] E. Suhir, A. Shakouri, Assembly Bonded at the Ends: Could Thinner and Longer Legs Result in a Lower Thermal Stress in a Thermoelectric Module Design?.", Journal of Applied Mechanics 79.6 (November 2012) (2012) 061010. doi:10.1115/1.4006597.

[55] P. Code, C. Prix, Photovoltaic concentrators (CPV) – Performance testing – Part 1: Standard conditions (2013).

[56] International Renewable Energy Agency, Renewable power generation costs in 2014, http://www.irena.org/DocumentDownloads/Publications/IRENA_RE_Power_Costs_2014_report.pdf (January 2015).

[57] J. Duffie, W. Beckman, Solar Engineering of Thermal Processes, 4th Edition, John Wiley & Sons, Ltd., 2003, pp. 163–165.

[58] B. Poudel, Q. Hao, Y. Ma, Y. Lan, A. Minnich, B. Yu, X. Yan, D. Wang, A. Muto, D. Vashaee, X. Chen, J. Liu, M. S. Dresselhaus, G. Chen, Z. Ren, High-thermoelectric performance of nanostructured bismuth antimony telluride bulk alloys., Science (New York, N.Y.) 320 (5876) (2008) 634–8. arXiv:arXiv:1011.1669v3, doi:10.1126/science.1156446.
URL http://www.ncbi.nlm.nih.gov/pubmed/18356488

[59] X. Yan, B. Poudel, Y. Ma, W. S. Liu, G. Joshi, H. Wang, Y. Lan, D. Wang, G. Chen, Z. F. Ren, Experimental studies on anisotropic thermoelectric properties and structures of n-type Bi2Te2.7Se0.3, Nano Letters 10 (9) (2010) 3373–3378. doi:10.1021/nl101156v.

[60] T. H. Kwan, X. Wu, Power and mass optimization of the hybrid solar panel and thermoelectric generators, Applied Energy 165 (2016) 297–307. doi:10.1016/j.apenergy.2015.12.016.

[61] S. Leblanc, S. K. Yee, M. L. Scullin, C. Dames, K. E. Goodson, Material and manufacturing cost considerations for thermoelectrics, Renewable and Sustainable Energy Reviews 32 (2014) 313–327. doi:10.1016/j.rser.2013.12.030.

[62] M. L. Olsen, E. L. Warren, P. A. Parilla, E. S. Toberer, C. E. Kennedy, G. J. Snyder, S. A. Firdosy, B. Nesmith, A. Zakutayev, A. Goodrich, C. S. Turchi, J. Netter, M. H. Gray, P. F. Ndione, R. Tirawat, L. L. Baranowski, A. Gray, D. S. Ginley, A high-temperature, high-efficiency solar thermoelectric generator prototype, Energy Procedia 49 (2013) 1460–1469. doi:10.1016/j.egypro.2014.03.155.

[63] The Engeneering ToolBox, Thermal conductivity of comon materials and gases, https://www.engineeringtoolbox.com/thermal-conductivity-d_429.html (September 2018).

[64] H. Liu, X. Xia, Q. Ai, X. Xie, C. Sun, Experimental investigations on temperature-dependent effective thermal conductivity of nanoporous silica aerogel composite, Experimental Thermal and Fluid Science 84 (2017) 67 – 77. doi:https://doi.org/10.1016/j.expthermflusci.2017.01.021. URL http://www.sciencedirect.com/science/article/pii/S0894177717300225

[65] R. Lamba, S. Manikandan, S. C. Kaushik, Performance Analysis and Optimization of Concentrating Solar Thermoelectric Generator, Journal of Electronic Materials 47 (9) (2018) 5310–5320. doi:10.1007/s11664-018-6410-7.

[66] B. Vermeersch, G. De Mey, A Fixed-Angle Dynamic Heat Spreading Model for (An)Isotropic Rear-Cooled Substrates, Journal of Heat Transfer 130 (12) (2008) 121301. doi:10.1115/1.2976557.

[67] K. Yazawa, A. Shakouri, Supporting Information cover sheet Cost-efficiency trade off and the design of thermoelectric power generators (2011) 1–11.

[68] F. Incropera, D. DeWitt, Fundamentals of heat and mass transfer, John Wiley & Sons Australia, Limited, 2002.

[69] W. Liu, H. S. Kim, Q. Jie, Z. Ren, Importance of high power factor in thermoelectric materials for power generation application: A perspective, Scripta Materialia 111 (2016) 3–9. doi:10.1016/j.scriptamat.2015.07.045.

[70] Y. C. Gerstenmaier, G. Wachutka, Thermoelectric converters with optimum graded materials and current distribution in one dimension and three dimensions, Physica Status Solidi (B) Basic Research 254 (7) (2017). doi:10.1002/pssb.201600690.

[71] W. Seifert, V. Pluschke, K. Zabrocki, Optimizing the electrical power output of a thermogenerator with the Gerstenmaier/Wachutka approach, Physica Status Solidi (A) Applications and Materials Science 211 (3) (2014) 685–695. doi:10.1002/pssa.201330176.